Research Article | Vol. 28, No. 13 / 22 June 2020 / Optics Express 19760
Optics EXPRESS

High harmonic generation in armchair carbon nanotubes

ÓSCAR ZURRÓN-CIFUENTES,* ROBERTO BOYERO-GARCÍA, CARLOS HERNÁNDEZ-GARCÍA, AND LUIS PLAJA

Grupo de Investigación en Aplicaciones del Láser y Fotónica, Departamento de Física Aplicada, University of Salamanca, E-37008, Salamanca, Spain
*ozurronci@usal.es

Abstract: We study high-order harmonic generation (HHG) in armchair-type single-wall carbon nanotubes (SWNTs) driven by ultrashort, mid-infrared laser pulses. For a SWNT with chiral indices (n, n), we demonstrate that HHG is dominated by bands $|m| = n - 1$ and that the cut-off frequency saturates with intensity, as it occurs in the case of single layer graphene. As a consequence, HHG in SWNTs can be described effectively as a one-dimensional periodic system, whose high-frequency emission can be modified through the proper control of the structural parameters. Additionally, we show that the HHG mechanism in nanotubes has some similarities to that previously reported in single layer graphene. However, as a main difference, the electron-hole pair excitation in SWNTs is connected to the non-adiabatic crossing through the first van Hove singularity of the $|m| = n - 1$ bands, instead of the crossing through the Dirac point that takes place in graphene.

1. introduction

Carbon nanotubes are carbon allotropes with quasi-one dimensional periodic structure. Their remarkable mechanical, electrical and thermal properties have attracted considerable interest since their discovery at the early 90's. They were first reported as carbon microtubules, made of concentric shells and diameters ranging from a few to several hundred nanometers [1]. Some years later, single-wall carbon nanotubes (SWNTs) were synthesized rolling monolayer graphene [2,3]. SWNTs have diameters around the nanometer and an extraordinarily perfect crystalline structure. SWNTs are also interesting topological objects, with electronic, optical and structural properties depending on the rolling direction (chiral angle) of the graphene sheet. These somewhat complex structures, which exhibit tens to hundreds of atoms in the unit cell, have well defined symmetries that easy the understanding of their physical properties [4,5].

Recently, the nonlinear optical response of periodic systems to intense mid-infrared radiation has captivated the interest of the scientific community. High-order harmonic generation (HHG) in crystalline solids has been a subject of interest already at the early days of the study of strong-field phenomena, either in realistic bulk solids [6] or dimensionally reduced models [7,8]. Experiments in crystalline solids subjected to intense fields have been demonstrated to emit high harmonics [9], resulting from the non-perturbative electronic response to the driving field. HHG has been extensively studied in atomic and molecular systems [10]. In gases, harmonics are radiated upon the recollision of electrons, that are first ionized, next accelerated and finally, redirected to the parent ion by the electromagnetic field [11,12]. The absence of a privileged resonance results in well defined *plateau* structures in the harmonic spectra extending up to cut-off frequencies at the extreme ultraviolet (UV) or even, at the soft x-rays regime [13,14]. In finite-gap solids, interband HHG follows a mechanism similar to that in gases or molecules, but ionization is replaced by the tunnel excitation from the valence to the conduction band, and the harmonic radiation occurs when the exited electron recombines with its hole [15]. Single layer (gapless) graphene has also been recently demonstrated to produce high order harmonics when interacting

#394714 https://doi.org/10.1364/OE.394714
Journal © 2020 Received 8 Apr 2020; revised 7 Jun 2020; accepted 8 Jun 2020; published 19 Jun 2020

Optics EXPRESS

with a strong mid-infrared (IR) field [16]. It has been shown that HHG in this system differs from bulk solids, as the first step (tunnel excitation) is replaced by electron-hole pair creation during the non-adiabatic crossing of the momentum-space trajectories near the Dirac points [17]. This fact introduces an extraordinary complexity, since the initiation of the HHG process is not linked to the field's amplitude maxima, when tunnel excitation is more likely. Graphene shows also an interesting non-linear anisotropy, allowing for photon spin conversion and ultrafast polarization changes in the emitted harmonic spectra [18].

Despite the considerable effort in the study of HHG in graphene and other 2D materials, similar studies for technologically feasible lower dimensional geometries —quasi 1D— are not abundant [19]. In this paper we present theoretical results of HHG in armchair-type SWNTs induced by few-cycle IR laser pulses. We demonstrate that, in this context, SWNTs behave effectively as one-dimensional two-band systems, whose properties can be modified with the choice of the SWNT's geometry. Remarkably enough, a recent experimental report shows that the high order harmonic emission spectra can be controlled either by tuning the electronic structure of SWNTs or carrier injection using electrolyte gating approaches, with up to the 11^{th}-order harmonic being observed in semiconductor tubes of relative large band gap ~ 1.26 eV [20].

The paper is organized as follows: First, we briefly review the structural characteristics of SWNTs, with special emphasis on their symmetries and the zone-folded electronic band structure. Next, in section 3 we present our method for the numerical integration of the time-dependent Schrödinger equation (TDSE) in SWNTs. In section 4 we present and discuss our results for the high harmonic spectra and, using a semiclassical model, we describe the HHG mechanism along with the dependence of the cut-off frequency with the intensity. Finally, we present our conclusions.

2. Structure of $\mathcal{A}$-type single-wall carbon nanotubes

For diameters above one nanometer, the effects of curvature can be neglected and the SWNT's electronic structure can be derived from that of single-layer graphene [21,22]. The nanotube corresponds to a graphene sheet rolled along the direction pointed by the chiral vector $\mathbf{C}_h = n_1\mathbf{a}_1 + n_2\mathbf{a}_2$, $(n_1, n_2) \in \mathbb{Z}^2$ being the tuple of chiral indices, and $\mathbf{a}_1 = a_0(\sqrt{3}/2, 1/2)$ and $\mathbf{a}_2 = a_0(\sqrt{3}/2, -1/2)$ the graphene's primitive vectors, with $a_0 = 2.46$ Å. The chiral indices (n_1, n_2) define the nanotube diameter $d_t = |\mathbf{C}_h|/\pi$, the chiral angle θ between $\mathbf{C}_h$ and $\mathbf{a}_1$, $0° \leq |\theta| \leq 30°$, and the translational period along the tube axis $a = \sqrt{3}a_0\sqrt{n_1^2 + n_1n_2 + n_2^2}/N_R$, where $N_R = \gcd(2n_1 + n_2, 2n_2 + n_1)$. $\mathcal{A}$-type —armchair— nanotubes correspond to chiral indices (n, n) and $|\theta| = 30°$, while $(n, 0)$ denotes $\mathcal{Z}$-type —zigzag— tubes, with $|\theta| = 0°$. Both zigzag and armchair tubes are achiral species, unlike $\mathcal{C}$ —chiral— nanotubes, where $n_2 \neq n_1$ $(n_i \neq 0)$.

Figure 1 shows the structure of a $(9, 9)$ armchair SWNT in (a) real and (b) reciprocal space, respectively. Symmetries of SWNTs are directly related to chirality. All nanotube species show a-period translational symmetry along the tube axis (z axis, by convention), a screw axis of pure rotational symmetries, which in the case of $\mathcal{A}$-type nanotubes coincides with the tube axis, and π-rotational symmetry around the U-axis, transverse to z. In addition, $\mathcal{Z}$ and $\mathcal{A}$-type tubes present mirror symmetries in the horizontal xy-plane (σ_h) and vertical yz-plane (σ_v). Figure 1(a) shows the essential symmetry elements of armchair nanotubes. Note that $\sigma_h = U \cdot \sigma_v$.

The translational periodicity implies the conservation of the quasi-momentum along the nanotube axis k. Besides, the rotational symmetry around the z-axis implies the conservation of m, the z-projection of the electron's orbital angular momentum. For $\mathcal{A}$-type nanotubes, the mirror reflection planes impose well-defined parities to the electronic states: the parity with respect to σ_v is denoted as A for even states, and B, for odd ones, while the parity under σ_h reflections is denoted by $\pm$ for even and odd states, respectively. Therefore, the state of the

Optics EXPRESS

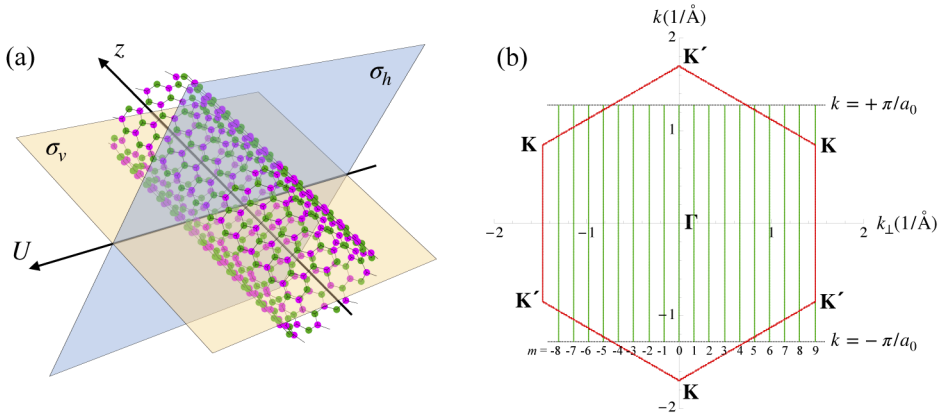

Fig. 1. (a) View of the structure and symmetries of a (9,9) armchair nanotutube. Magenta and green circles represent the atoms in the two sublattices of the unrolled graphene sheet. (b) Allowed **k** vectors in the first Brillouin zone of (9,9) armchair tube (green lines). This nanotube has 36 C-atoms in its unit cell, $q = 18$, $m = 0, \pm1, \pm2, \ldots, \pm8, 9$ and $d_t = 12.2$ Å. The red hexagon shows the boundary of the graphene's BZ along with the high symmetry points K and Γ.

electron corresponds to a particular irreducible representation of the line group, characterized by the set $\{k, m, A/B, \pm\}$.

Curvature effects being neglected, SWNT's Brillouin zone (BZ) can be constructed from graphene's using the zone-folding approach, i.e. considering the nanotube as graphene with periodic boundary conditions along the circumferential direction [4,5]. As a result, the BZ of the nanotube corresponds to a set of q —the number of hexagons in the unit cell— straight lines with length $2\pi/a$, parallel to the tube axis and separated by constant distances $2/d_t$. Each line is labelled by the index m, which takes integer values in $(-q/2, q/2]$. As an example, Fig. 1(b) depicts the BZ of (9,9) armchair. Note that for $\mathcal{A}$-type tubes, the translational period is $a = a_0$.

Within the nearest-neighbor tight-binding approximation, the energy dispersion is given by $E_\pm(\mathbf{k}) = \pm\gamma|f(\mathbf{k})|$, where $\gamma = 2.97$ eV is the hopping parameter and $f(\mathbf{k})$ the complex function

$$f(\mathbf{k}) = e^{-ia_0k_\perp/\sqrt{3}}\left(1 + 2e^{i\sqrt{3}a_0k_\perp/2}\cos\frac{a_0k}{2}\right), \tag{1}$$

being $k_\perp = 2m/d_t$ the set of wave vectors along the circumferential direction. Figure 2 shows the band structure of the (9,9) nanotube. Bands are labelled according to the value of $|m|$ and the parities upon the vertical and horizontal mirror symmetries, A/B and $+/-$ respectively. Bands with $m = 0$ and 9, drawn in black, are singlets with + parity, while the rest of bands are doubly degenerated in the interval $a_0k \in [0, \pi)$, with $E = A$ or B parity, and converge at $a_0k = \pi$. For $ka_0 = 0$ all states have + parity. $\mathcal{A}$-type (n, n) nanotubes are semimetals, as both valence and conduction bands are degenerated at the point $a_0k = \pm2\pi/3$ of the band $m = n$, corresponding to the Dirac points K and K' of the graphene's Brillouin zone, see Fig. 1(b). The density of states (DOS) profile is shown as a shaded area in the background of Fig. 2. Van Hove singularities correspond to points where the slope of the energy bands is null.

Optics EXPRESS

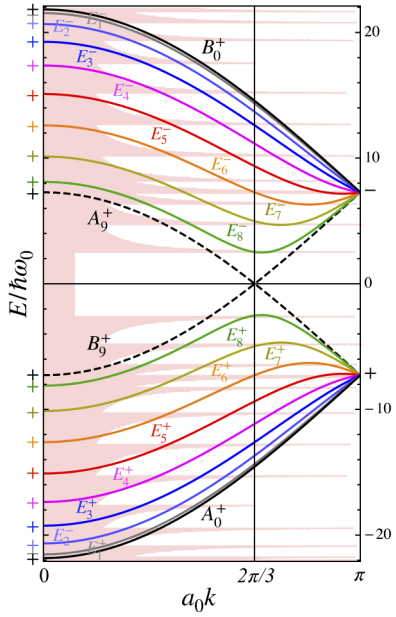

Fig. 2. Band structure of (9,9) armchair. The energy is given in units of the frequency of a 3μm driving field ($\hbar\omega_0 = 0.41$ eV). The horizontal axis represents the wave vector times the translational period a_0. The solid (dashed) black lines indicate the $m = 0$ ($m = 9$) singlets. The rest of the bands represent double degenerated states $E^{\pm}_{|m|}$, with $E = A/B$. Parities under σ_h reflections at $a_0k = 0$ and π are also indicated. The pink-filled profile in the background shows the density of states, dominated by the van Hove singularities.

3. Interaction with an electromagnetic field

Symmetries of $\mathcal{A}$-type SWNTs impose selection rules for the optical transitions between electronic states. If the incident electric field is linearly polarized along the nanotube axis, optical transitions are essentially vertical, conserve m and A/B, while swap $\pm$. As a result, transitions $A_0^+ \to B_0^+$ and $B_n^+ \to A_n^+$ are forbidden in any (n,n) $\mathcal{A}$-type tube. The rest of transitions involving bands $|m| = 1,\ldots,n-1$ are allowed for any $a_0k \in (0,\pi]$, but they are forbidden at $a_0k = 0$. Furthermore, the electronic intraband dynamics are also subjected to the *Umklapp* rule $m' = m \pm n \pmod{2n}$, so that m shifts to m' when the first Brillouin zone is exceeded through $a_0k = \pi$ [4,23].

Let us consider an $\mathcal{A}$-type SWNT being irradiated by a laser pulse $\mathbf{F}(t)$ linearly polarized along the direction of its axis. Within the dipole approximation, the interaction is described by the time-dependent Hamiltonian $H(t) = H_0 - q_eF(t)z$, where q_e is the elementary charge. If $\Phi_m^{\pm}(k;\mathbf{r})$ are the eigenstates of the conduction and valence bands, the time-dependent wavefunction can be expressed as:

$$\Psi(\mathbf{r},t) = \sum_m \int \Psi_m(k;\mathbf{r},t)dk = \sum_m \int \left[C_m^+(k,t)\Phi_m^+(k;\mathbf{r}) + C_m^-(k,t)\Phi_m^-(k;\mathbf{r})\right] dk. \tag{2}$$

As shown for graphene in [17], introducing the oscillating frame $\hbar\kappa_t = \hbar k - q_eA(t)/c$, where $A(t)$ is the vector potential, and using the transformation:

$$C_m^M(\kappa_t,t) = C_m^+(\kappa_t,t) - C_m^-(\kappa_t,t) \tag{3}$$

$$\tilde{C}_m^P(\kappa_t,t) = e^{-i\phi_m(\kappa_t)}\left[C_m^+(\kappa_t,t) + C_m^-(\kappa_t,t)\right], \tag{4}$$

Optics EXPRESS

the dynamical equations can be written in the following form:

$$i\hbar\frac{d}{dt}C_m^M(\kappa_t,t) = \frac{E_m^+(\kappa_t)+E_m^-(\kappa_t)}{2}C_m^M(\kappa_t,t) + \frac{E_m^+(\kappa_t)-E_m^-(\kappa_t)}{2}e^{i\phi_m(\kappa_t)}\tilde{C}_m^P(\kappa_t,t) \tag{5}$$

$$i\hbar\frac{d}{dt}\tilde{C}_m^P(\kappa_t,t) = \frac{E_m^+(\kappa_t)+E_m^-(\kappa_t)}{2}\tilde{C}_m^P(\kappa_t,t) + \frac{E_m^+(\kappa_t)-E_m^-(\kappa_t)}{2}e^{-i\phi_m(\kappa_t)}C_m^M(\kappa_t,t), \tag{6}$$

where $E_m^{\pm}$ is the energy of the valence (-) and conduction (+) bands with index m, and ϕ_m is the phase of the complex function $f(\mathbf{k})$ in Eq. (1). The harmonic emission is then proportional to the second derivative of the emission dipole, which is given by:

$$d(t) = i\frac{q_e}{2}\sum_m\int\left[C_m^{M*}\frac{\partial C_m^M}{\partial\kappa_t} + \tilde{C}_m^{P*}\frac{\partial\tilde{C}_m^P}{\partial\kappa_t}\right]dk. \tag{7}$$

In addition, we compute the intraband fraction of the harmonic spectra as:

$$a_m^{\text{intra}}(t) = \frac{q^2}{\hbar^2}F(t)\int\left[|C_m^+|^2\frac{\partial^2E_m^+}{\partial\kappa_t^2} + |C_m^-|^2\frac{\partial^2E_m^-}{\partial\kappa_t^2}\right]dk. \tag{8}$$

4. Results and discussion

Equations (5), (6), (7) and (8) have been integrated numerically considering mid-IR 8-cycle driving pulses. The electric field is assumed linearly polarized along the nanotube axis and defined as $F(t) = F_0\sin^2(\pi t/8T)\sin(\omega_0 t)$ for $0 \le t \le 8T$ and 0 at any other t, being F_0 the field's amplitude, T the period, and $\omega_0 = 2\pi/T$ the frequency. The beam is aimed perpendicularly to the nanotube, thus traversing an atomic-size thickness and therefore, we neglect propagation effects.

Figure 3 shows the calculated HHG yield from (9,9) $\mathcal{A}$-tube at a driving peak intensity of 5×10^{10} W/cm^2 and 3 μm wavelength. The pulse duration is 28 fs (2.9 cycles) at full width at half maximum (FWHM), which is smaller than the decoherence time due to carrier collisions [24–26]. Figure 3 shows clearly the emergence of a spectral plateau extending up to a cut-off frequency, which corresponds to the seventh harmonic. Note that the intensity used here is about two-orders of magnitude below the "transition intensity" to non-perturbative HHG, predicted in 1D models [7]. Only odd-order harmonics are present in the spectrum, as a consequence of centrosymmetric structure of the system. All harmonics are linearly polarized in the direction of the tube axis.

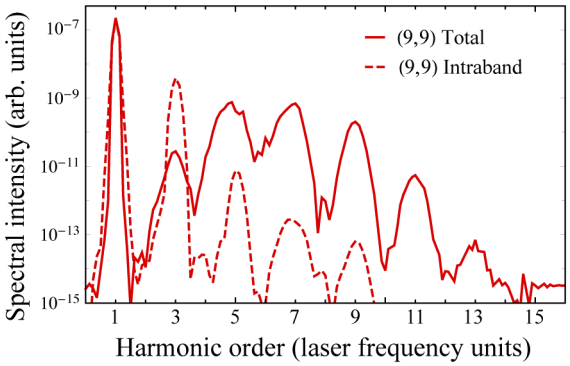

Fig. 3. The solid line represents the total harmonic yield from (9,9) $\mathcal{A}$-tube driven by a 3μm wavelength, 28 fs (2.9 cycles) FWHM pulse at 5×10^{10} W/cm^2 peak intensity. The dotted line indicates the intraband spectral component.

Optics EXPRESS

We can analyze the contribution of the different m bands to the harmonic spectra by considering the specific form of the component parallel to the nanotube axis of the interband matrix element in the length gauge [27–29]:

$$D_m(k) = -\frac{a_0 q_e}{2} \frac{\sin\left(\frac{a_0 k}{2}\right) \sin\left(\frac{m\pi}{n}\right)}{1 + 4\cos\left(\frac{a_0 k}{2}\right)\left[\cos\left(\frac{m\pi}{n}\right) + \cos\left(\frac{a_0 k}{2}\right)\right]}. \tag{9}$$

Figure 4(a) shows the magnitude of the matrix element $|D_m(k)|$ in the $(9,9)$-armchair tube for different band indices m. Consistent with the symmetry considerations discussed above, $|D_m(k)|$ is null for $m = 0, 9$. As a consequence, the contribution of these bands to the total HHG corresponds solely to the intraband dynamics. For the rest of bands, the coupling shows peaks of magnitude increasing with $|m|$, corresponding to the first four van Hove singularities in the DOS. The absolute maximum of $|D_m(k)|$ is reached at the first van Hove singularity. This suggests that the interaction with the driver laser is much stronger for the states packed at the first van Hove singularity than for others and therefore, that the interband emission spectra is mainly due to transitions within such states. Note that the increased band curvature near the Dirac points entails sharper van-Hove singularities and, therefore, enhances the efficiency of the interband transitions in HHG. In contrast, 1D models with finite gaps demonstrate intraband currents as the main source of harmonic radiation [30]. This behavior is further illustrated in Fig. 4(b), where

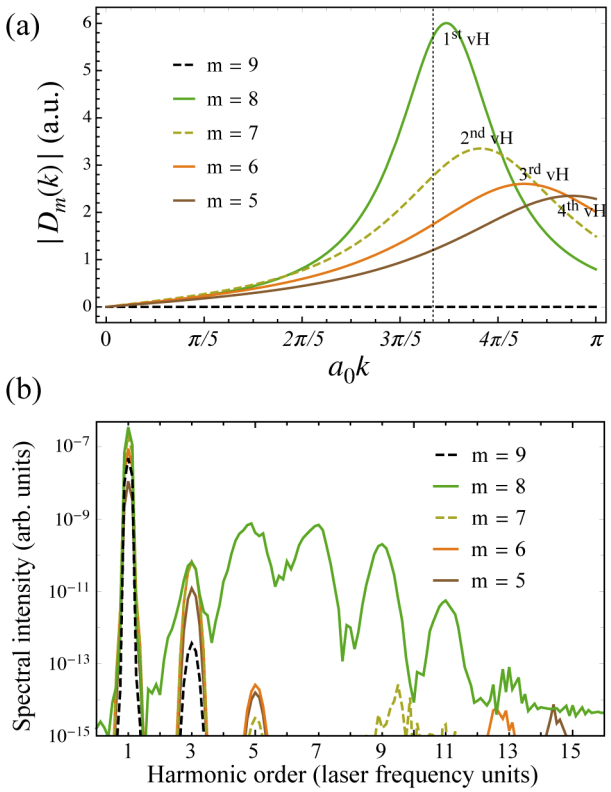

Fig. 4. (a) Matrix element $|D_m(k)|$ corresponding to the (9,9) armchair tube for different m values. The dotted line at $a_0k = 2\pi/3$ indicates the band's crossing point for $m = 9$. (b) Contribution to the harmonic yield from the different values of m. The driver's parameters are the same as in Fig. 3.

Optics EXPRESS

we show the different contributions to the emission spectra from the (9,9)-$\mathcal{A}$-tube corresponding to several values of m. The coherent addition of the contributions from all m-values gives the spectrum shown in Fig. 3. Nevertheless, note that the higher order harmonics are given by the contribution from the slices $|m| = 8$ of the Brillouin Zone shown in Fig. 1(b), which are connected with the first van Hove singularity. The other points of the BZ, where $|D_m(k)|$ and the curvature of the bands are weaker, contribute to the lower order harmonics mainly with intraband radiation. Note that the band gap at the first van Hove singularity is near resonant with a $5\omega_0$ transition, thus enhancing the interband component of the high harmonic emission.

Figure 5 shows the harmonic yield from several $\mathcal{A}$-tubes of different diameters. The basic features of the spectra are maintained, although the efficiency of the higher order harmonics in the spectral non-perturbative area (5^{th} and 7^{th}) increases with the tube diameter. Note that the slope of the bands closest to $a_0k = 2\pi/3$ increases with the tube diameter, which implies that the number of electronic states available at the maximal values of $D_m(k)$ also increases. Also, the value of $|D_m(k)|$ approaches the singularity at the Dirac points, which explains the higher efficiency of the harmonics. It is also observed that, as the diameter increases, the 5^{th} harmonic is red-shifted since the resonance with the gap energy of the $m = n - 1$ band is reduced. Note that the cut-off barely changes, independently of the size of the nanotube.

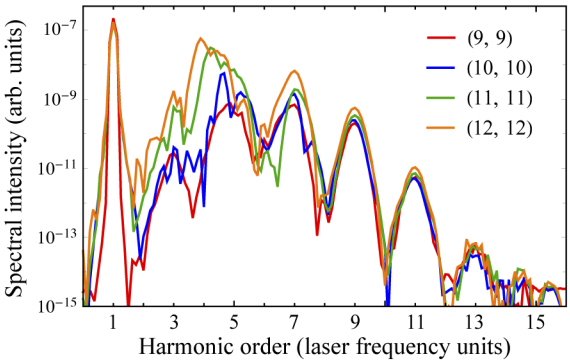

Fig. 5. Harmonic yield from (9,9), (10,10), (11,11) and (12,12) armchair tubes. The diameters of these tubes are $d_t = 1.22, 1.36, 1.50$ and 1.63 nm, respectively. The electric field parameters are those in Figs. 3 and 4(b).

Figure 6(a) shows the spectral yield from the (9,9) $\mathcal{A}$-tube irradiated by a driving pulse of the same duration and wavelength, but with peak intensity of 5×10^{12} W/cm^2. As intensity increases, the spectral *plateau* is extended towards the extreme UV. In Fig. 6(b) we show the scaling of the cut-off frequency with the driving field intensity. The filled area in the background corresponds to intensities above the damage threshold, assuming that the damage threshold fluence is 150 mJ/cm^2 [31]. Note that the cut-off frequency saturates at the largest intensities to a photon energy of $\simeq 16.7$ eV, which is the gap corresponding to the maximum oscillation of the coupled quasimomentum κ_t. This saturation has also been described in graphene [17] and in gap semiconductors [32].

The spectral features of the radiated harmonics can be described in semiclassical terms. For this purpose we use the saddle-point approach model (SPAM) introduced for single layer graphene [17,33]. The SPAM demonstrated that the high-harmonic spectra in graphene results from the recombination of electron-hole pairs, created during the non-adiabatic crossing of the Dirac points by the electron trajectories. For the description of SWNTs, we shall replace this condition by the non-adiabatic crossing through the first van Hove singularity. In nanotubes, therefore, the SPAM describes the q-th order harmonic emission as the Fourier transform of the dipole

Optics EXPRESS

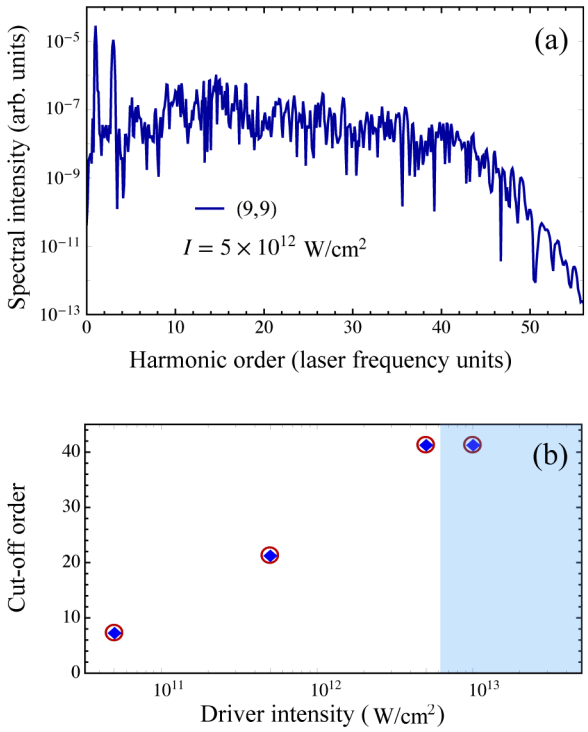

Fig. 6. (a) Harmonic yield from (9,9) $\mathcal{A}$-tube driven by a 3μm wavelength, 28 fs (2.9 cycles) FWHM pulse at 5×10^{12} W/cm^2 peak intensity. (b) Cut-off scaling with intensity from (9,9) armchair. The blue diamonds are the result of the numerical integration of the TDSE. The red circles are predicted by the semiclassical SPAM considering electron-hole creation at the first van Hove singularity: $a_0 k = 2\pi/3$, $m = 8$. The filled area in the background corresponds to intensities above the damage threshold.

acceleration, computed from the k-space integral:

$$\tilde{d}_m^{\updownarrow}(q\omega_0) = i\frac{\mathcal{D}_0^m}{q_e}\int_k\int_{-\infty}^{\infty} e^{\frac{i}{\hbar}[S_m(k,t,t_H)+q\hbar\omega_0 t]} D_m(\boldsymbol{\kappa}_t)dkdt, \tag{10}$$

where $S_m(k,t,t_H) = \int_{t_H}^{t}\left[E_m^+(\kappa_\tau) - E_m^-(\kappa_\tau)\right]d\tau$, $\mathcal{D}_0^m$ is a constant, and t_H is the time of crossing the first van Hove singularity, when the electron-hole pairs are generated. Taking into account that the main contributions to the integral in Eq. (10) are the stationary-phase points [15,33,34], from saddle-point analysis we find that the harmonic emission occurs when the following conditions are fulfilled:

$$\int_{t_H}^{t} v_m^+(\kappa_\tau)d\tau = \int_{t_H}^{t} v_m^-(\kappa_\tau)d\tau, \tag{11}$$

and

$$E_m^+(\kappa_t) - E_m^-(\kappa_t) = q\hbar\omega_0, \tag{12}$$

where $v_m^{\pm}(\kappa_t) = \frac{1}{\hbar}\frac{\partial}{\partial k}E_m^{\pm}(\kappa_\tau)$ are the velocities of the valence and conduction band electrons. In this semiclassical framework, conditions (11) and (12) define the generation mechanism for HHG in SWNTs: (i) as a consequence of the interaction with the field, the electron initially at point k in the valence band oscillates with amplitude $\kappa_t - k$; (ii) at time t_H the electron crosses the first van Hove singularity, where D_m reaches its maximal value, and is promoted to the conduction band,

Optics EXPRESS

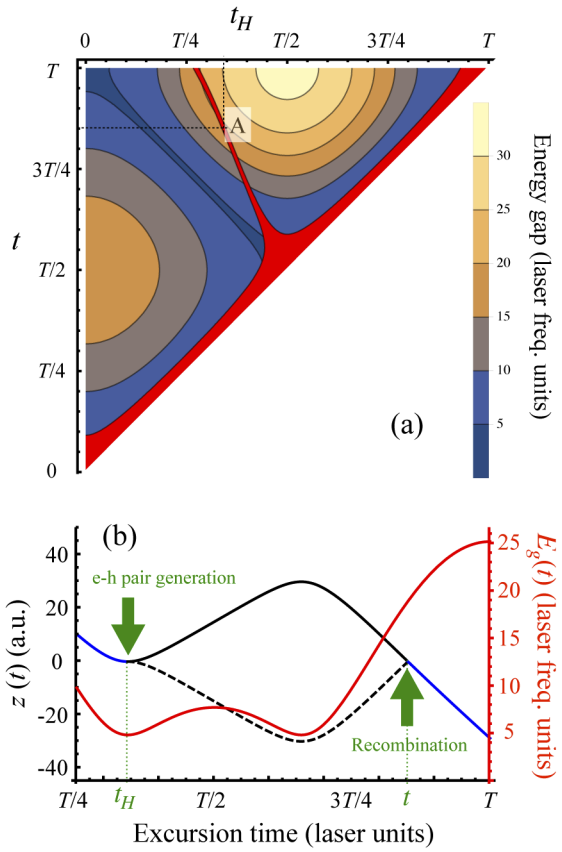

Fig. 7. (a) Map of the energy of the emitted photon for different classical trajectories computed with the SPAM, being t_H the time of creation of the electron-hole pair and t the potential time of the photon emission. The points where the electron-hole trajectories intersect in direct space at time t are represented by the red area. (b) Electron and hole trajectories corresponding to point A illustrated in panel (a). The trajectories of the electron (black solid line) and the hole (dashed line) are represented as a function of time. The red curve represents the energy gap $E_g(t)$ between the electron and the hole during their oscillation in the bands. The figure corresponds to a driving laser pulse of 3 μm wavelength with constant intensity of 5×10^{11} W/cm^2 targeting a (9,9) armchair tube.

leaving a hole; (iii) according to Eq. (11), the electron-hole pair will quiver in the momentum space until time t, when their trajectories intersect in the real space; and (iv) upon recombination, a photon resonant with the band gap at κ_t is emitted, thus fulfilling Eq. (12).

The SPAM predicts that the maximum energy of the photon emission will be the maximum gap experienced by the electron-hole pair during its oscillation in the reciprocal space. For (n, n) tubes, the first van Hove singularity is located at the band $m = n - 1$ and therefore, this band holds the relevant contribution to the total HHG, as shown in Fig. 4(b). If the driving pulse is strong enough, the electron-hole pair originated in the band $m = n - 1$ will eventually exceed the first Brillouin zone at $a_0 k = \pi$ and shift the oscillation to band $m = 0$ according to the *Umklapp* rule. In particular, for (9,9) $\mathcal{A}$-type tubes the maximum gap experienced by the electron-hole pairs created at $m = 8$ corresponds to 16.7 eV, which matches with the value of the saturated cut-off energy shown in Fig. 6(b). As the nanotube diameter increases, the contributions from

Optics EXPRESS

the second and third van Hove singularities become more relevant, increasing the efficency of the HHG (as shown Fig. 5).

Figure 7(a) shows a map of the energy gap experienced by an electron-hole pair, created at the first van Hove singularity in time t_H, as a function of time t. The map corresponds to a 3 μm wavelength pulse with constant intensity of 5×10^{11} W/cm^2 targeting an (9,9) $\mathcal{A}$-tube, thus representing in a simple way the phenomenology during the cycle of maximum amplitude of the 8-cycle laser pulse considered above for the quantum mechanical model. The red-colored areas correspond to electron-hole trajectories created at t_H that overlap in the same unit cell in the real space at time t. As an example, in point A the electron-hole pair is created at $t_H \simeq 0.35T$ and emits a $\simeq 19\hbar\omega_0$ photon when recombined at $t \simeq 0.85T$. Figure 7(b) shows the classical trajectories of this electron. Note that, for the laser parameters in Fig. 7(a), the maximal photon energy is given by the highest contour constrained to the red-colored area. Therefore, we can use these kind of maps to identify the cut-off frequency of the HHG spectra at each intensity and wavelength. Figure 6(b) shows a comparison between the SPAM cut-off prediction (red circles) and the results of the exact integration of TDSE (blue diamonds). Both results are in excellent agreement.

Additionally, we show in Fig. 8 the SPAM energy map at 3 μm wavelength for a pulse of larger intensity 10^{13} W/cm^2. As it also happens in single layer graphene [17], when the driver's intensity increases, the topology of the red-colored region becomes more complex, so the same harmonic may be emitted by two or more sets of trajectories within the same half cycle of the field. In particular, note that Fig. 8 shows four sets of contributions, labelled from a to d, for the maximum (cut-off) frequency.

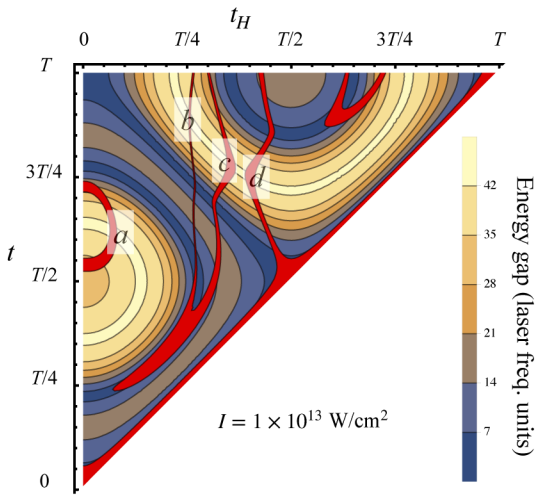

Fig. 8. Energy map for the emitted harmonic photon from a (9,9) armchair tube according to SPAM for a driver peak intensity of 10^{13} W/cm^2. The points corresponding to intersecting electron-hole trajectories are highlighted in red.

5. Conclusions

We have studied the non-perturbative emission of armchair (n, n) carbon nanotubes irradiated by intense few-cycle infrared laser pulses, both from the numerical integration of the TDSE and using a semiclassical model. We have found that the harmonic spectrum follows the typical non-pertubative characteristics, a *plateau* followed by a cut-off frequency. We show that high-harmonics are generated mainly from interband —valence to conduction— transitions

Optics EXPRESS

between nanotube bands with index $|m| = n - 1$. According to our semiclassical model, HHG is initiated by electrons initially quivering in the valence band, that are promoted to the conduction band during the non-adiabatic excursion across the first van Hove singularity. This first step shares similarities with the case of graphene, and departs strongly from the tunnel picture, valid for atoms, molecules and bulk solids. After the excitation to the conduction band, the generated electron-hole pair evolves under the influence of the electric field. The harmonic emission takes place upon recombination of the pair when both electron and hole overlap in real space. In comparison with graphene, HHG in nanotubes is constrained by their one-dimensional nature, i.e. the discrete nature of the reciprocal space: nanotubes with larger diameters emit harmonics more efficiently, since the $|m| = n - 1$ band is closer to the Dirac points, the first van Hove singularity becomes more pronounced and the dipole matrix element is increased. Our semiclassical model predicts the scaling of the harmonic cut-off frequency with the driving field intensity and fully characterizes the electron-hole pairs' creation and recombination times leading to the emission of harmonics. The results presented in this manuscript may be extended in future works to the analysis of the influence of chirality and driver's polarization on the high harmonic emission spectra.

Funding

Junta de Castilla y León, European Regional Development Fund(SA287P18); Ministerio de Ciencia, Innovación y Universidades (FIS2016-75652-P, RYC-2017-22745, PID2019-106910GB-I00); European Research Council (851201).

Acknowledgments

The authors acknowledge V. Marcos for exciting infusions. This project has received funding from the European Research Council (ERC) under the European Union's Horizon 2020 research and innovation program.

Disclosures

The authors declare no conflicts of interest.

References

1. S. Iijima, "Helical microtubules of graphitic carbon," Nature **354**(6348), 56–58 (1991).
2. S. Iijima and T. Ichihashi, "Single-shell carbon nanotubes of 1 nm diameter," Nature **363**(6430), 603–605 (1993).
3. D. S. Bethune, C. H. Klang, M. S. de Vries, G. Gorman, R. Savoy, J. Vazquez, and R. Beyers, "Cobalt-catalysed growth of carbon nanotubes with single-atomic-layer walls," Nature **363**(6430), 605–607 (1993).
4. S. Reich, C. Thomsen, and J. Maultzsch, *Carbon nanotubes: basic concepts and physical properties* (WILEY-CVH Verlag GmbH & Co. KGaA, 2004).
5. L. E. F. Foa-Torres, S. Roche, and J. C. Charlier, *Introduction to graphene-based nanomaterials: from electronic structure to quantum transport* (Cambridge University, 2014).
6. L. Plaja and L. Roso, "High-order harmonic generation in a crystalline solid," Phys. Rev. B **45**(15), 8334–8341 (1992).
7. F. H. M. Faisal and J. Z. Kamiński, "Floquet theory of high-harmonic generation in periodic structures," Phys. Rev. A **56**(1), 748–762 (1997).
8. K. A. Pronin, A. D. Bandrauk, and A. A. Ovchinnikov, "Harmonic generation by a one-dimensional conductor: Exact results," Phys. Rev. B **50**(5), 3473–3476 (1994).
9. S. Ghimire, A. D. DiChiara, E. Sistrunk, P. Agostini, L. F. DiMauro, and D. A. Reis, "Observation of high-order harmonic generation in a bulk crystal," Nat. Phys. **7**(2), 138–141 (2011).
10. L. Plaja, R. Torres, and A. Zaïr, *Attosecond Physics. Attosecond Measurements and Control of Physical Systems* (Springer-Verlag, 2013).
11. P. B. Corkum, "Plasma perspective on strong field multiphoton ionization," Phys. Rev. Lett. **71**(13), 1994–1997 (1993).
12. K. J. Schafer, B. Yang, L. F. DiMauro, and K. C. Kulander, "Above threshold ionization beyond the high harmonic cutoff," Phys. Rev. Lett. **70**(11), 1599–1602 (1993).

Optics EXPRESS

13. J. L. Krause, K. J. Schafer, and K. C. Kulander, "High-order harmonic generation from atoms and ions in the high intensity regime," Phys. Rev. Lett. **68**(24), 3535–3538 (1992).
14. T. Popmintchev, M. C. Chen, D. Popmintchev, P. Arpin, S. Brown, S. Alisauskas, G. Andriukaitis, T. Balciunas, O. Mücke, A. Pugzlys, A. Baltuska, B. Shim, S. E. Schrauth, A. Gaeta, C. Hernández-García, L. Plaja, A. Becker, A. Jaron-Becker, M. M. Murnane, and H. C. Kapteyn, "Bright Coherent Ultrahigh Harmonics in the keV X-ray Regime from Mid-Infrared Femtosecond Lasers," Science **336**(6086), 1287–1291 (2012).
15. G. Vampa, C. R. McDonald, G. Orlando, D. D. Klug, P. B. Corkum, and T. Brabec, "Theoretical Analysis of High-Harmonic Generation in Solids," Phys. Rev. Lett. **113**(7), 073901 (2014).
16. N. Yoshikawa, T. Tamaya, and K. Tanaka, "High-harmonic generation in graphene enhanced by elliptically polarized light excitation," Science **356**(6339), 736–738 (2017).
17. O. Zurrón, A. Picón, and L. Plaja, "Theory of high-order harmonic generation for gapless graphene," New J. Phys. **20**(5), 053033 (2018).
18. O. Zurrón-Cifuentes, R. Boyero-García, C. Hernández-García, A. Picón, and L. Plaja, "Optical anisotropy of non-perturbative high-order harmonic generation in gapless graphene," Opt. Express **27**(5), 7776–7786 (2019).
19. S. de Vega, J. D. Cox, F. Sols, and F. J. García de Abajo, "Strong-field-driven dynamics and high-harmonic generation in interacting one dimensional systems," Phys. Rev. Res. **2**(1), 013313 (2020).
20. H. Nishidome, K. Nagai, K. Uchida, Y. Ichinose, Y. Yomogida, K. Tanaka, and K. Yanagi, "*Control of high-harmonic generation by tuning the electronic structure and carrier injection*," arXiv:2004.11000v1 [physics.optics] (2020).
21. N. Hamada, S. I. Sawada, and A. Oshiyama, "New one-dimensional conductors: Graphitic microtubules," Phys. Rev. Lett. **68**(10), 1579–1581 (1992).
22. R. Saito, M. Fujita, G. Dresselhaus, and M. S. Dresselhaus, "Electronic structure of chiral graphene tubules," Appl. Phys. Lett. **60**(18), 2204–2206 (1992).
23. N. Bozović, I. Bozović, and M. Damnjanović, "Selection rules for polymers and quasi-one-dimensional crystals: IV. Kronecker products for the line groups isogonal to Dnh," J. Phys. A: Math. Gen. **18**(6), 923–937 (1985).
24. M. Breusing, C. Ropers, and T. Elsaesser, "Ultrafast Carrier Dynamics in Graphite," Phys. Rev. Lett. **102**(8), 086809 (2009).
25. J. M. Iglesias, M. J. Martín, E. Pascual, and R. Rengel, "Carrier-carrier and carrier-phonon interactions in the dynamics of photoexcited electrons in graphene," J. Phys.: Conf. Ser. **647**, 012003 (2015).
26. D. Brida, A. Tomadin, C. Manzoni, Y. J. Kim, A. Lombardo, S. Milana, R. R. Nair, K. S. Novoselov, A. C. Ferrari, G. Cerullo, and M. Polini, "Ultrafast collinear scattering and carrier multiplication in graphene," Nat. Commun. **4**(1), 1987 (2013).
27. S. V. Goupalov, "Optical transitions in carbon nanotubes," Phys. Rev. B **72**(19), 195403 (2005).
28. S. V. Goupalov, A. Zarifi, and T. G. Pedersen, "Calculation of optical matrix elements in carbon nanotubes," Phys. Rev. B **81**(15), 153402 (2010).
29. H. K. Kelardeh, V. Apalkov, and M. I. Stockman, "Wannier-Stark states of graphene in strong electric field," Phys. Rev. B **90**(8), 085313 (2014).
30. D. Golde, T. Meier, and S. W. Koch, "High harmonics generated in semiconductor nanostructures by the coupled dynamics of optical inter- and intraband excitations," Phys. Rev. B **77**(7), 075330 (2008).
31. A. Roberts, D. Cormode, C. Reynolds, T. Newhouse-Illige, B. J. LeRoy, and A. S. Sandhu, "Response of graphene to femtosecond high-intensity laser irradiation," Appl. Phys. Lett. **99**(5), 051912 (2011).
32. G. Vampa and T. Brabec, "Merge of high harmonic generation from gases and solids and its implications for attosecond science," J. Phys. B: At., Mol. Opt. Phys. **50**(8), 083001 (2017).
33. A. Nayak, M. Dumergue, S. Kühn, S. Mondal, T. Csizmadia, N. G. Harshitha, M. Füle, M. U. Kahaly, B. Farkas, B. Major, V. Szaszkó-Bogár, P. Földi, S. Majorosi, N. Tsatrafyllis, E. Skantzakis, L. Neoričić, M. Shirozhan, G. Vampa, K. Varjú, P. Tzallas, G. Sansone, D. Charalambidis, and S. Kahaly, "Saddle point approaches in strong field physics and generation of attosecond pulses," Phys. Rep. **833**, 1–52 (2019).
34. M. Lewenstein, P. Balcou, M. Y. Ivanov, A. L'Huillier, and P. B. Corkum, "Theory of high-harmonic generation by low-frequency laser fields," Phys. Rev. A **49**(3), 2117–2132 (1994).